Inertial instabilities in a microfluidic mixing-separating device

Allysson F. Domingues,[1] Robert J. Poole,[1] and David J. C. Dennis[1]
School of Engineering, University of Liverpool, Liverpool, L69 3GH, UK

(Dated: 11 June 2019)

Combining and separating fluid streams at the micro-scale has many scientific, industrial and medical applications. This numerical and experimental study explores inertial instabilities in so-called mixing-separating micro-geometries. The geometry consists of two straight square parallel channels with flow from opposite directions and a central gap that allows the streams to interact, mix or remain separate (often also referred to as the *H-geometry*). Under creeping-flow conditions (Reynolds number tending to zero) the flow is steady, two-dimensional and produces a sharp interface between fluid streams entering the geometry from opposite directions. When Re exceeds a critical value, one of two different supercritical, inertial instabilities appears which leads to significant changes in the flow pattern and an increased level of interaction between the two streams, although the flow remains steady. The exact form of the instability is dependent on the gap size and Reynolds number and we identify two distinct instabilities, one of which appears in devices with large gaps and another which appears in devices with small gaps. At intermediate gap sizes both instabilities can occur in the same device (at different onset Re). The experimental results for one gap size are used to validate our numerical method, which is then applied to a wider range of gap sizes. The results suggest that gap size is of primary importance in determining the type of instability that occurs. With a judicious choice of gap size, the instabilities can be exploited (or avoided) in scientific, medical or other microfluidic applications.

I. INTRODUCTION

Microfluidic devices have had a significant impact on the biomedical, pharmaceutical, food and chemical industries[1]. With the increasing use of micro- and nano-scale devices across the biomedical industry, especially within biomedical diagnostics and chemical fields[1–4], the ability to mix two fluid flows or manipulate particles on the micro- and nano-scale has become an enticing field of research. Due to the necessarily small scale of these devices ($\leq 1000\mu m$), inertial forces are usually small, and laminar flow is predominant. Consequently, the fluid mixing process in the micro-geometries often relies on molecular diffusion, which is notably inefficient when compared to turbulent convective mixing[1,5]. Additionally, biological and chemical analysis is typically concerned with molecules and bio-particles with small dimensions. Subsequently, positioning and separating particles in micro and nanofluidic devices creates many challenges[2,6]. Different devices (or geometries) have historically been tested to improve mixing performance and characterise flow behaviours providing a greater understanding of the governing mechanisms at this scale, as well as the possibilities within this field of research.

Microfluidic devices have previously been tested both experimentally and numerically across a variety of geometries such as: a T-shaped planar channel with two square opposing inlets and a perpendicular outlet of equal combined area, i.e. maintaining a constant bulk velocity in each channel arm[7]; a serpentine curved channel where the fluid motion is in a different direction to the axis of curvature due to the existence of a secondary motion[8]; a cross-slot – planar crossed channel in which two opposed incoming fluid streams impinge on each other, and leave through opposite channel exits[9–11]; and another simple configuration with potential applications in micro and nano-scale flows is the microfluidic mixing-separating cell (also referred to as the *H-geometry*) – two straight square parallel channels with flow from opposite directions interacting through a central gap that allows the streams to mix or remain separate[12]. When compared to a cross-slot, a mixing-separating cell shows many similarities in the fluid motion. The cross-slot device with one pair of aligned arms rotated by 90° towards the other pair would lead to a mixing-separating cell with $\sqrt{2}H$ gap size at the centre of the device (where H is the height=width of the channel). It is well known that cross-slot devices are sensitive to an inertial instability at modest Reynolds numbers[13]. This instability can often be employed to enhance mixing and heat transfer, offering an efficient alternative to geometry modification or external forcing[14].

In this work we explore the inertial instabilities and changes in flow topology in a mixing-separating microfluidic device. We perform both experiments (using flow visualisation) and numerical simulations in a specific geometry with a gap size of five times the channel height ($g = 5H$). Finding good agreement between the experiments and simulations, we further utilise the simulation technique to explore the effect of varying the gap size (g). We demonstrate that both the nature of the instability and the Re at which it occurs varies as the gap size is changed.

A. Passive mixing using microfluidic devices with impinging flow streams

Micromixers homogenise fluids in small volumes (nano- or microliters), very limited space and satisfactory timescales[15]. Active mixing schemes implement an external force to the microfluidic mixing system other than the fluid flow, typically by way of a mechanical transducer.

Ultrasonic transducers have been shown to improve the mixing performance in mixers by stirring the samples. This method of external excitation generates considerable heat in addition to the system, which alters the reactivity between materials and is difficult to account for in analysis[1]. Passive microfluidic mixers, studied in this paper, rely on fluid mechanical behaviour induced by geometry and the physical properties of the flow to enhance mixing. As the fluid flow passes through such devices, inertia-driven instabilities induce mixing. Therefore, by studying this complex effect on the flow, stability diagrams can be constructed, and more efficient mixing devices proposed. In a different application, studies suggest the use of laminar vortices for particle entrapment, and it has appeared as an attractive biomedical tool. Investigations on a vortical flow cell separation platform show that finite size cancer cells could be captured in a confined cavity microfluidic device as an effect of hydrodynamic forces on vortical laminar flow. As the red blood cells are almost unaffected by these forces due to their small size, the device represents a biomedical application for the inertial instability as it can isolate the cancer cells from blood for liquid biopsy[6,16].

Many investigations[7,17–24] on a micro T-shaped mixer were performed to improve fluid mixing between two streams flowing at a "low" Reynolds number ($Re \lesssim 200$). This design has flow entering the channel from two opposite inlets and then reaching a stagnation point before turning 90° and being expelled down the outlet channel. At a critical Reynolds number a symmetry-breaking bifurcation occurs[25]. The behaviour of the flow after this instability has been shown to increase the mixing performance within microfluidic devices[26]. Three different regimes of laminar flow (symmetric stratified flow, symmetric vortex flow, and, beyond the instability, the so-called *engulfment flow* regime, which is asymmetric) were observed depending on the Reynolds number in the outflow mixing channel[7,17,19,20]. Sarkar et al.[27] conducted numerical simulations to evaluate mixing performance when varying the angle of the opposing inlet channels in a T-junction microfluidic device. The computational approach has been validated using experimental and theoretical data. The results suggest that mixing performance is found to be dependent on the angle between the two inlet arms.

The cross-slot geometry consists of perpendicular, bisecting channels with opposing inlets and outlets. This arrangement creates a flow field with a stagnation point located at its centre[28]. The design is simple, allows ease of control, and has motivated an extensive range of applications in several scientific fields for the mixing of fluids[9,14,29,30]. For Newtonian fluid streams imposed at opposite inlets a flow bifurcation occurs at a critical Reynolds number, the flow remains steady, but becomes asymmetric, and a spiral vortex develops as the two streams spiral around each other (rather like the engulfment flow regime in the T-channel)[14]. For this type of instability, the maximum transverse velocity component on the horizontal centreline at the centre of the cross is commonly used as a bifurcation parameter as it is zero before the onset of the instability and becomes non-zero when the vortex appears[13,14,31].

Results from previous work on the cross-slot show that the instability exhibits hysteretic behaviour, and the symmetry-breaking bifurcation is a subcritical pitchfork[14]. The critical Reynolds number encountered when increasing Re and decreasing Re is different. Haward et al.[13], Burshtein et al.[32], and Zografos et al.[31] reported similar critical Reynolds numbers ($Re_c \approx 40$) with decreasing Re when using a cross-slot geometry with aspect ratio, $AR = 1$ (squared ducts). While for increasing Re, the onset of the instability occurred at $Re_c \approx 46$[13,31]. Notably, the hysteresis in the numerical simulations depends on the level of noise and therefore on many factors (for instance, the numerical solver, numerical method, and mesh size applied).

A variation of the cross-slot geometry is a device with an X-shaped junction where the angle between inlet and outlet channels is less than the 90° of the cross-slot. This has been studied by experimentally by Cachile et al.[33] for angles between 10° and 90°. Their primary focus was the proportion of fluid from each inlet reaching each outlet and how this varied with the geometric angle of the X-shaped junction. Recently Correa et al.[34] studied an X-geometry where the channel cross-section was circular, unlike the square (or rectangular) cross-section studied in our (and much of the previously discussed) work. They investigated several angles between 15° and 90° using three-dimensional (3D) simulations. A variety of vortical structures were observed depending on the angle of the junction and the Reynolds number. Just like the cross-slot is the extreme case of an X-junction where the angle between the channels is 90°, it is notable that the mixing-separating geometry we study here is an extreme case of the X-geometry where the angle is 0° (or 180° depending on your point of view). However, the mixing-separating geometry was not considered by Correa et al.[34] or Cachile et al.[33].

B. The mixing-separating device (H-geometry)

Previous work on mixing-separating cells, shows that a vortical behaviour occurs and becomes more complicated with increasing Reynolds number. Originally proposed by Cochrane, Walters, and Webster[35] and Walters and Webster[36], numerical simulations ($1 < Re < 50$) showed that the size and strength of a central vortex increased as Re is increased, eventually splitting into two vortices at a relatively high Re. It was found that a wider central gap (g) encourages flow to reverse its direction and exit from a different outlet[36]. This means the fluid tends to cross from one channel to the other. Experimentally, laser flow-visualisation results were limited to a small range of Reynolds numbers ($Re < 8$) for a wide-gap (five times the height of the channel, $g = 5H = 25$mm) and

for a medium-gap ($g = 3H = 15$mm), Re was limited to 25. The experimental apparatus consisted of peristaltic pumps to drive the flow and a catch-and-weigh apparatus to determine the flow rate. The channels were made of aluminium with height of 5mm and depth of 20mm. The unavailability of a very refined mechanism for controlling the flow rates with sufficient accuracy was reflected in unbalanced flow streams within the inlets which resulted in differences between numerical and experimental data Walters and Webster [36].

Humphrey and Li [37] presented an unusual characteristic of the flow inside the mixing-separating cell while increasing Re ($300 < Re < 1000$) experimentally from a stationary state (from rest). By using water and methylene blue as a dye, a tilted interface delineated the streams a few seconds after starting the flow from rest. This two-dimensional (2D) interface soon transformed into a 3D unsteady flow. The authors suggest that transverse pressure gradients imposed by the main motion are responsible for the inclined (tilted) flow interface at low Reynolds number, and the three-dimensional phenomenon appears as a consequence of spanwise vorticity. Motivated by this experimental outcome, Humphrey et al. [38] used a numerical technique to extensively investigate the vortical behaviour previously noticed in their work. The study was limited to relatively high values of Re ($100 < Re < 300$) where the flow is unstable and time-dependent.

The overall aim of the present paper is to harness a greater understanding of the inertial flow instabilities when varying the gap size in a mixing-separating microfluidic device (hence low Re). The characterisation of the flow before and after the bifurcation helps to predict the flow topology and locate the position and orientation of vortex structures within the device, which consequently benefits the design of microfluidic devices to manipulate flow conditions using laminar vortices (e.g. for particle entrapment or mixing).

II. EXPERIMENTS

A. Experimental set-up

A schematic diagram of the experimental rig is shown in figure 1. The channels were micro-machined using CNC machining in brass and encased in polyoxymethylene (an insulating material also known as ACETAL). A 6.5mm thick upper wall fabricated from borosilicate glass provides a good seal and optical access. Each channel cross-section is square, $H = W = 500\mu\text{m} \pm 1\mu\text{m}$, the gap is $g = 5H = 2.5$mm, and the wall separating the channels is $a = H/5 = 100\mu$m. The rig is mounted on an inverted microscope (DMI, Leica Microsystems GmbH) fitted with a filter cube (excitation BP $530 - 545$nm, dichroic mirror 565nm, barrier filter $610 - 675$nm, Leica Microsystems GmbH). A pulsed Nd:YAG laser (Solo-PIV III laser, wavelength 532nm, 50mJ per pulse, New Wave Research) is used to excite the dyed fluid, and a CCD camera enables direct observation of the $x-y$ plane. (The origin is placed at the geometric centre of the device.) The camera field of view (FOV) is 3.2mm x 2.4mm and thoroughly covers the central region of the device containing the gap. The camera is synchronised with the laser at a repetition rate of 8.875Hz. All images shown in this work were captured using an 8x microscope objective (Leica Microsystems GmbH).

The cross-section dimensions of the mixing-separating cell flow device were quantified using a Nikon EPIPHOT TME inverted microscope with 100 times magnification, 235 pixels = 500μm. The combined length of the channel inlet and outlet is $80H$ ($L = 40 \pm 0.1$mm) to ensure fully-developed flow at the central region of the geometry for all Reynolds numbers studied[39]. Four cylindrical holes (with a diameter and depth of 10mm) at the end of each arm of the mixing-separating cell were drilled and tapped so that pressure tappings could be incorporated.

Flow through the microfluidic system was driven using two identical pressure vessels, which are connected to a compressed air supply. Both pressure vessels were maintained at room temperature. The flow rate was measured for each inflow using a metal tube flowmeter (3750A Ar-Mite Low Flow Armored Flowmeter, BROOKS). According to the manufacturer, the flowmeter measurement accuracy is 5% of the full scale. The metal tube flowmeter was experimentally calibrated by comparison to a syringe pump (PHD Ultra Harvard Apparatus), which has a certified accuracy of 0.35%, in the range $3 - 80$ml/min. This comparison indicated that the flow rate obtained using the metal tube flowmeter shows good agreement with that obtained using the syringe pump, with an average deviation of approximately 3.5%. The liquid flows through the device and is ultimately ejected into the collecting container. The collected liquid is then weighed instantaneously as a function of time $W(t)$ by a Mettler Toledo (Delta Range, TOLEDO) SB16001 balance (sampling rate of 5Hz and uncertainty ± 0.1g at range of 3200g or below) connected to the computer via a serial port (RS-232C), allowing for a precise measurement of the amount of working fluid collected for a known time. The time-averaged fluid discharge rate ($\dot{m}$) is estimated as $\Delta W/\Delta t$. The mass balance technique provides a very accurate measurement of the flow rate through the device, whereas the two flow meters are used to balance the flow rate of the two streams during the experiment. This balancing is non-trivial, but it is important as it was observed that a slight imbalance in the flow rate between the two streams could significantly affect the resulting flow.

A diaphragm-type differential pressure transducer (DP15-26, Validyne Engineering) with a quoted full-scale accuracy of $\pm 0.25\%$ was employed for measuring the pressure differential between the inlet and outlet of the channel cells combined with a flexible Tygon tube (internal diameter 1 mm). A diaphragm-sensing element model $3 - 42$ with pressure range $0 - 140$kPa was utilised

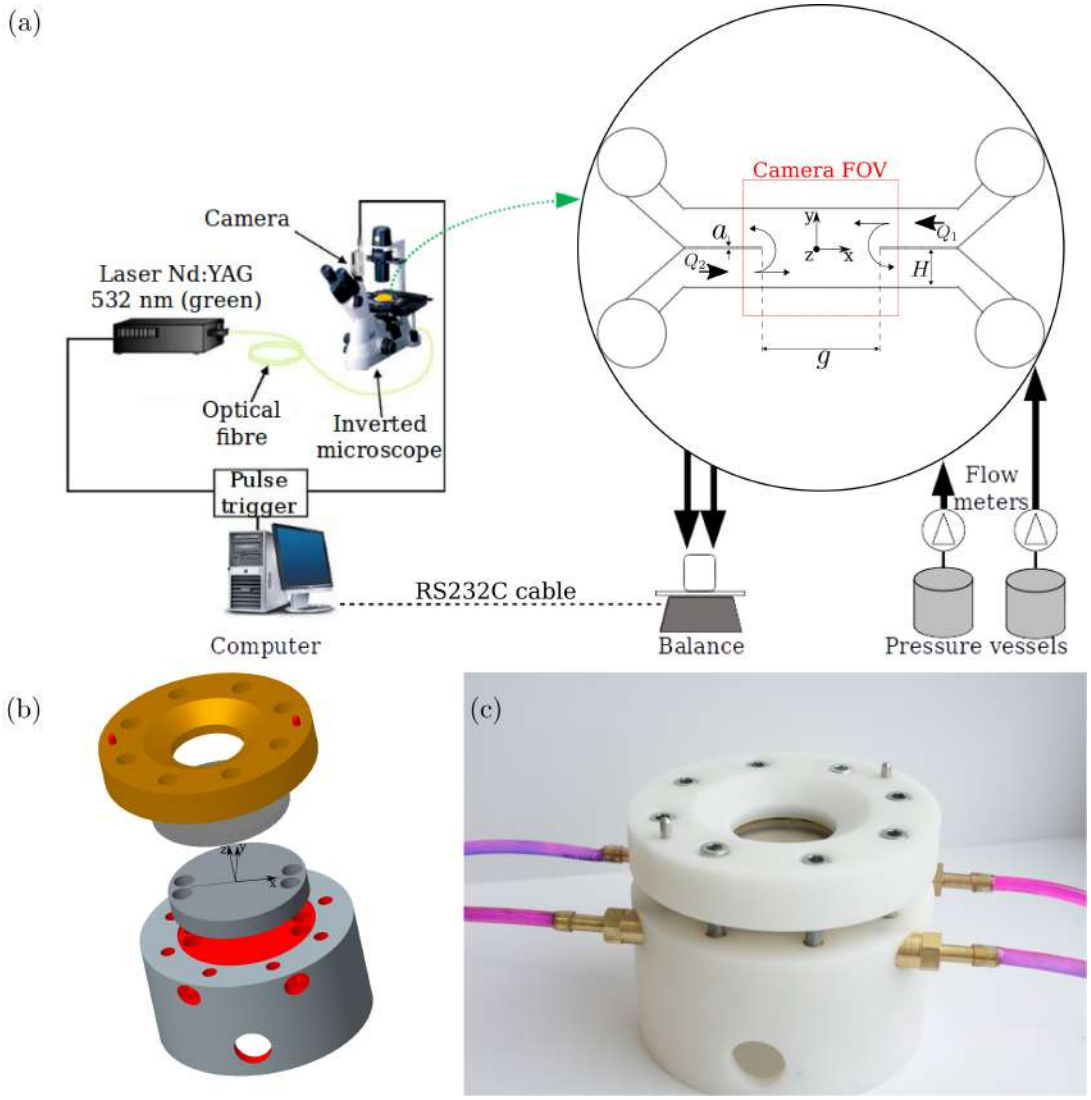

FIG. 1. (a) Schematic of the microfluidic mixing-separating device (not to scale). (b) An exploded view of the microfluidic device. (c) Photograph illustrating the fully assembled experimental rig.

for the pressure-drop measurements. The voltage output for the pressure transducer, which was digitised using a Validyne CD223 digital transducer indicator, was sampled by an analogue-to-digital converter (ADC) at 100 Hz for 60 seconds. The pressure transducer was calibrated at periodic intervals using air against an MKS Baratron differential pressure transducer (MKS Instruments Inc. USA). Minor pressure losses (the inlet and outlet manifolds and corresponding sudden contraction and expansion) associated with the measured pressure drop are estimated using the traditional relationships used in microscale[40,41] where the percentage of these losses to the major pressure drops ranges from just 0.11% at a low flow rate to 2.3% at a high flow rate. Thus, the pressure drop across an individual inlet/outlet pair was approximately equal to that across the mixing-separating device itself.

The flow visualisation technique consists of pumping dyed fluid (see §II B) from one of the inlets while undyed fluid is pumped in the other inlet; both inlets are kept at the same flow rate (monitored by the flow meters on each arm). Fluid motion starts from rest and, after reaching steady-state conditions in approximately 10 seconds, at least fifty images were captured for each measurement. As the flow at all conditions investigated was steady, these fifty individual images were essentially identical (except for measurement noise). However, fifty images were always taken to check that the flow was time-independent (as we did not know a priori the Re at which time-dependent flow would occur). They could also be used to average away random noise (which was minimal).

The Reynolds number of the flow is defined in equation (1), based on the bulk velocity ($U_b = \dot{m}/\rho H^2$) and the

TABLE I. The measured values of density and viscosity of the working fluid in the range of temperatures relevant to the experiments.

Temperature	Density (ρ)	Viscosity (μ)
°C	kg/m^3	$Pa.s$
20	1183.6	0.0215
22	1183.1	0.0201
24	1182.5	0.0186

channel height (H),

$$Re = \frac{\rho U_b H}{\mu} \tag{1}$$

where ρ and μ are the density and the dynamic viscosity of the working fluid respectively.

B. Working fluid

The working fluid used for the experimental measurements was a mixture of glycerine (relative density 1.26, ReAgent Chemical Services) and distilled water with a nominal concentration of 70 per cent glycerine (by weight). Rhodamine-B (ACROS Organics) was used as a fluorescent dye to enable flow visualisation[42–44]. The dyed fluid was prepared by dissolving 0.05g (500 ppm) of Rhodamine-B in one litre of working fluid. The density (ρ) and viscosity (μ) of the mixed solution were measured at room temperature (varying from 20°C to 26°C) as shown in table I. A density meter (Anton Paar DMA 35N) with a quoted precision of 0.001g/cm^3 was used for quantifying the fluid density. A controlled-stress torsional rheometer (Anton Paar MCR302) was utilised to measure the fluid viscosity using a 60mm and 1° cone with a shear rate range from 1s^{-1} to 100s^{-1} (there was no variation of viscosity with shear rate as expected). The measured values of the density and dynamic viscosity are given in table I.

III. NUMERICAL SIMULATIONS

Numerical simulations were performed to match the gap size and conditions of the experimental mixing-separating device in order to validate the method. Subsequently, devices with a variety of gap sizes were investigated solely numerically in order to explore the influence of gap size.

A. Governing equations and numerical method

The fluid flow was assumed incompressible, isothermal, laminar, single phase, and steady-state. The fluid properties are assumed constant and temperature independent. The governing equations for continuity (Eq. 2) and momentum (Eq. 3) are:

$$\nabla \cdot u = 0 \tag{2}$$

$$\rho(u \cdot \nabla u) = -\nabla p + \mu \nabla^2 u \tag{3}$$

where ρ and μ, constant physical properties, represent density and dynamic viscosity respectively, u represents the velocity vector and p represents the pressure.

The computational domain consists of two opposed square channels interacting through a gap of non-dimensional width $\theta = g/H$ in the middle of a thin separating wall of non-dimensional thickness $\alpha = a/H$ (refer to figure 1). The combined length of the inlet and outlet channels was defined as 80 times its height ($L = 80H$). This length ensures that the flow is hydrodynamically fully-developed before it reaches the region of interaction for all Reynolds numbers studied[39].

The simulations were carried out using the finite-volume method within ANSYS Fluent Workbench version 14.5.7[45]. A modified SIMPLE algorithm developed by Patankar and Spalding[46] was employed for solving the equations in discretised form (pressure-velocity coupling scheme). The equations of momentum are solved with a second-order upwind scheme. A Neumann boundary condition (zero diffusion flux for all flow variables and an overall mass balance correction) was used at the outlets and no-slip conditions at all the walls. All the simulations were iterated until the convergence criteria of all relevant residuals fell to less than 10^{-10}.

Preliminary simulations were conducted with identical conditions to the experiments. The density and viscosity were constant and equal to the experimentally measured values (table I). Subsequently the system was non-dimensionalised, such that arbitrary reference values could be used, and it was found (as expected) that the non-dimensional system produced identical results to the simulations that matched the experiments. All further simulations were conducted with the arbitrary, non-dimensional system.

B. Computational meshes

A mesh refinement investigation was conducted to estimate the numerical accuracy of the simulations. A preliminary series of simulations were carried out with five different uniform hexahedral (all quad) computational meshes (shown in table II). The different meshes vary the number of cells across the cross-section with grid resolutions at the $y-z$ plane of 10x10, 20x20, 25x25, 30x30 and 50x50. Along the channel length (x direction), a fixed number of 100 cell divisions was applied accompanied by a biased refinement rate towards the geometry centre (bias factor, the ratio of the largest edge to the smallest edge, of 100:1). At the centre of the geometry,

TABLE II. Mesh convergence study. The error represents the percentage error between the value of v_{max}/U_b for the mesh compared to the value of v_{max}/U_b using the most dense mesh tested (M5).

Mesh	Cross-section	v_{max}/U_b	Error (%)	Number of cells
1	10x10	1.387	5.73	84000
2	20x20	1.450	1.48	380000
3	25x25	1.457	0.96	593750
4	30x30	1.464	0.51	855000
5	50x250	1.471	-	2375000

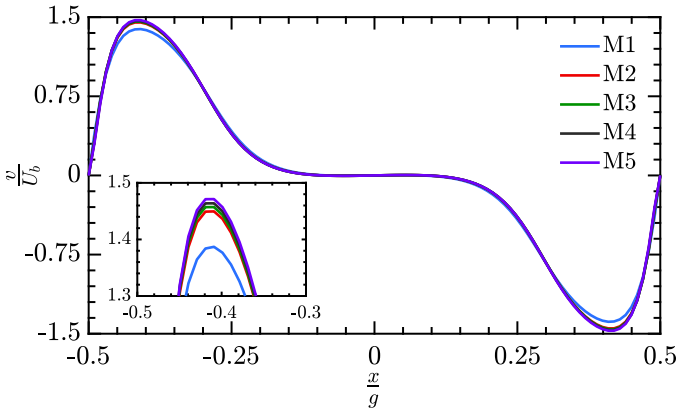

FIG. 2. The profile of v/U_b along the length of the gap (centreline along x-direction at $y = 0$ and $z = 0$) for the different meshes at a fixed Reynolds number ($Re = 30$). The inset zooms into the region around the maximum value of v/U_b.

where the gap is located, the grid is most refined and all control volumes are cubes.

Figure 2 shows the variation of the velocity profile associated with the v-component of velocity (i.e. the velocity component in the y-direction) with increasing mesh refinement for a typical simulation ($Re = 30$). The values were obtained along the gap horizontal centreline on the $x - y$ plane at $z = 0$ and normalised by the bulk velocity (U_b). The chosen criterion to determine the accuracy is the maximum value of the v across the gap between the channels (v_{max}/U_b). Firstly, it can be noted that the variation of v_{max}/U_b between the meshes becomes less than 1% when increasing the number of cells above 600,000 in the cross-section. The study revealed that mesh M4 had suitable characteristics for further simulations due to the low percentage error (0.51%) and reasonable number of cells (855,000) considering computational expense (see table II).

C. Bifurcation parameters and vortex identification method

A flow bifurcation parameter is required to define when an instability occurs and to characterise its nature. In a cross-slot micro-device, Haward et al.[13] adopted the maximum transverse velocity component, w (i.e. the velocity component in the z-direction), recorded along the horizontal centreline on the central plane as an instability growth parameter (w_{max}/U_b), which adequately described the onset and the evolution of the instability as the transverse velocity field breaks its symmetry after the bifurcation and a complex three-dimensional (3D) spiral vortex structure develops. However (as will be shown), this method is inadequate to define all the instabilities we discovered in the mixing-separating device.

An additional bifurcation parameter is used in this manuscript in order to characterise instabilities that are not manifest in w_{max}/U_b. The vortex identification method proposed by Zhou et al.[47], called the swirling strength criterion, has been utilised as it can adequately identify vortex structures in the flow. Using this method, the imaginary part of the complex-conjugate eigenvalue of the velocity gradient tensor (λ_{ci}) can be used to identify the presence and strength of a swirling motion. We interrogate the flow for vortices on the x-y plane ($z = 0$) of the geometry in the region of the gap, hence the local planar (2D) velocity gradient tensor (∇u) in Cartesian coordinates is defined as,

$$\nabla u = \begin{bmatrix} \frac{\partial u}{\partial x} & \frac{\partial u}{\partial y} \\ \frac{\partial v}{\partial x} & \frac{\partial v}{\partial y} \end{bmatrix}. \tag{4}$$

In this work, we use this technique to identify and quantify the vortices associated with one of the instabilities in the mixing-separating device. By considering the maximum normalised strength of this swirling motion, quantified by $\lambda_{ci}H^2/\nu$, (where ν is the kinematic viscosity of the working fluid, i.e. μ/ρ) in the plane of interest, one can adequately quantify the onset and the evolution of the instability with varying Re.

IV. EXPERIMENTS AND SIMULATIONS USING A WIDE GAP ($g = 5H$)

A. Friction factor

The pressure drop (Δp) between inflow and outflow arms (after subtracting the minor pressure losses as already discussed in §II A) and mean fluid flow velocity (U_b) were experimentally measured to determine the Darcy friction factor-Reynolds number product, fRe:

$$fRe = \frac{2\Delta p H^2}{L U_b \mu} \tag{5}$$

where L is the combined length of the inflow and outflow channels. The experimental measurements of friction factor-Reynolds number product versus Reynolds number are shown in figure 3. The uncertainty of fRe (denoted by error bars), which is associated with the measurement error of each term in Eq. 5, is carefully estimated by following the same methodology adopted

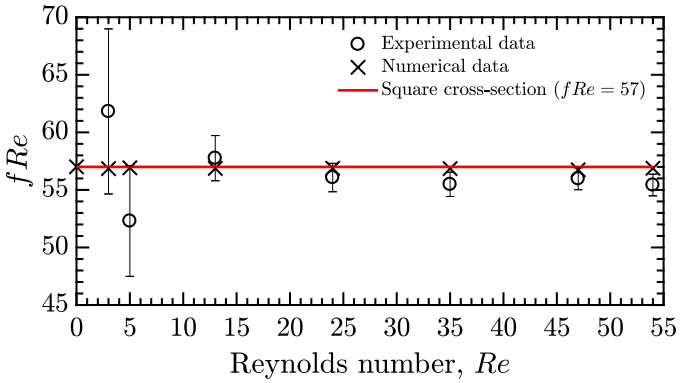

FIG. 3. Friction factor-Reynolds number product (fRe) as a function of Reynolds number for a mixing-separating device with $g = 5H$. For $Re < 5$, there are large relative uncertainties. Above $Re = 5$ the experimentally measured values agree well with the numerical simulations and the theory for a straight square channel

in Abed et al.[14]. The minimum and maximum uncertainty values of fRe are 1.7% and 11.6%, respectively. The large relative uncertainties occur at low flow rates where the small pressure drops generate a significant degree of error (approximately 90% of the total error of the fRe when $Re < 5$). Dimensional inaccuracies (particularly in measuring H) also play a significant role in the determination of fRe[40,48].

The experimental measurements of fRe were compared to the conventional theory for a fully-developed flow in a straight channel of a square cross-section ($fRe = 57$ in laminar flow, Shah and London[49]). When $Re > 5$, the measurements show acceptable agreement with this theoretical value. In this range, the maximum deviation between the measured values of fRe and Darcy's equation is within 3%. The results for $Re > 5$ are also in good agreement with the numerical simulations (which agree with the theory as expected). The pressure drop in the mixing-separating device therefore behaves essentially as flow in a straight channel and any additional pressure loss due to the gap, even after the onset of the instability ($Re > 30$), is small and within our measurement uncertainty. For very low Reynolds numbers ($Re < 5$), there is a significant degree of error in the measured pressure-drop data which can be attributed to the large relative uncertainties at low flow rates and small pressure drops.

B. Visualisation of the base flow

Figure 4 shows flow visualisation using one inlet stream dyed with rhodamine (white) and one inlet stream undyed (black) with the simulated flow pathlines at $z = 0$ superimposed. The numerical simulations and experimental results show virtually identical flow patterns indicating a very good agreement between the two methods.

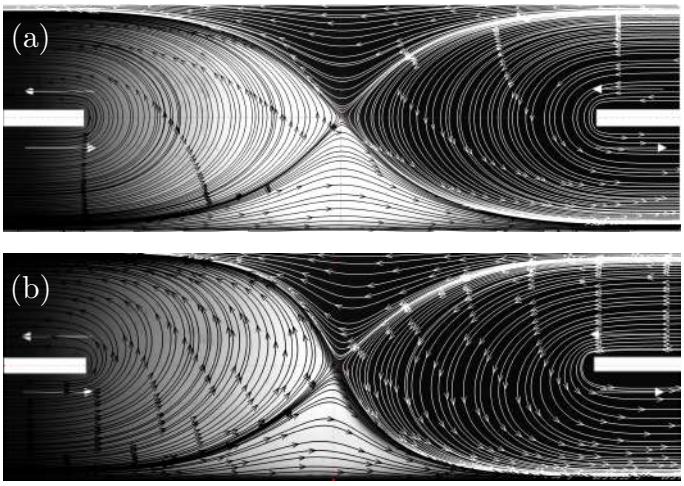

FIG. 4. Experimental flow visualisation images with one rhodamine-tinted stream (white) and one undyed stream (black) prior to the onset of any instability. (a) $Re = 2$, and (b) $Re = 29$. The experimental visualisations are superimposed with pathlines at the centre plane of the geometry from the equivalent simulations.

For a range of Re from 2 to 29, experimental and numerical results clearly show the majority of the fluid reverses through 180° in order to exit the device and only a small amount of fluid takes a path straight through the "H".

A distinct tilted interface between the dyed and undyed streams is visible for $Re \leq 29$. The effect of incrementally increasing the Reynolds number from 2 to 29 increases the angle of the interface with respect to the x axis. Figure 5 shows the evolution of the interface with increasing Re. By using the raw grey-scale image, binarising, cropping to the gap width and applying an edge detection technique, the interface between the two fluid streams can be located (see figure 5b-d). A small deviation in the flow balance between the two streams produced minor variations of the interface position within the "H", hence X_0 and Y_0 represent small adjustments to relocate the interface to the geometric centre for all Re to enable a proper comparison.

Under approximately creeping flow conditions, the vast majority of the flow turns around the corner of the separating wall and only a small part of the flow heads straight down the outlet of the channel, dividing the inlet flow stream in two at the stagnation point. With increasing Re, the interface between flow streams at the gap becomes more inclined and, consequently, more and more fluid reverses its direction. Above $Re = 29$, when the interface is approximately coincident with the y-axis, a vortex appears at the centre of the mixing-separating cell indicating the onset of an instability, although the flow remains steady.

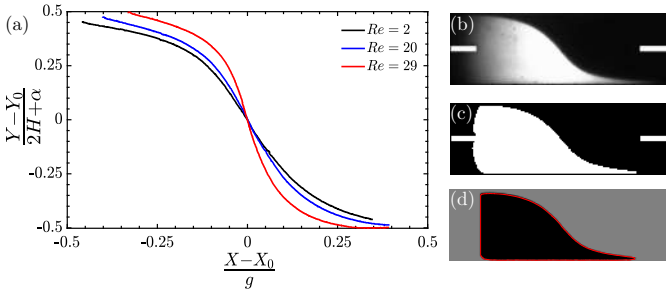

FIG. 5. (a) The interface between the two fluid streams for different Re obtained using edge detection, showing an increase in interface angle (with respect to the x-axis) with increasing Re. Image processing phases identifying edges between the two streams at $Re = 2$: (b) raw figure, (c) binary image and (d) edge detection.

C. Visualisation of the inertial instability

Figure 6 shows experimental flow visualisations and simulated streamlines for Re from 29 to 60. At $Re = 30$, just above the onset, a single vortex is present spanning the entire width of the cell. With increasing Re, it divides into a pair of co-rotating vortices (as in the numerical example shown at $Re = 40$). Figure 6d illustrates the vortices when $Re = 60$. Noticeably, with increasing Re, the two vortices separate. It is important to note that the flow remains steady and the vortex structure does not change in time for a fixed value of the Reynolds number. Unlike in the base flow, where a small portion of the flow passed straight through the device, after the onset of the instability, none of the flow takes the path to opposite exit, in addition there is a far greater mixing of the two streams due to the central vortex (or vortices at higher Re).

The results from numerical simulations and experiments agree well regarding the onset (Re_c) of the instability. However, one can observe small deviations in the comparative flow visualisations, particularly an absence of perfect rotational symmetry in the experimental results for $Re = 30$ and $Re = 40$ (figure 6). A small discrepancy in the flow balance between the two inlets explains this lack of symmetry. Precise matching of the flow rates on the different inlet channels to a high level of accuracy is not straightforward (despite the use of separate flowmeters on both inlets), whereas for the numerical simulations it is trivial to set identical boundary conditions and therefore obtain the perfect rotational symmetry.

As suggested by Humphrey et al.[38] and verified by our present numerical work, for a large enough Reynolds number ($Re > 185$) the flow becomes time-dependent. However, a detailed study of the time-dependent behaviour of this flow is beyond the scope of the present work, particularly as we are mainly interested in flow at low Re.

D. Characterisation of the instability from experiments

To quantify the onset and growth of the instability in the experimental data, the method suggested by Stroock et al.[5], and also employed by Haward et al.[13], was adopted to evaluate the level of interaction between the incoming fluid streams (M) in the central region of the device. By computing the root-mean-square (RMS) of the pixel intensity variation within the vortex region of the experimentally obtained images such as those shown in figure 6, we quantify the amount of interaction between the two incoming streams within the gap region as,

$$M = \sqrt{\frac{\sum_{i=1}^{n}(I_i - \langle I \rangle)^2}{n}}. \tag{6}$$

where I_i is the grayscale intensity value at pixel i, and $\langle\rangle$ indicates an average across all n pixels in the defined area of interest (example shown by yellow box in figure 6b).

Figure 7 presents the experimental quantification of the interaction between the two streams (using this M-parameter) as a function of the Reynolds number for the mixing-separating device with $g = 5H$. At Re close to the onset of the instability the growth of M follows the square root behaviour typical of a supercritical instability. The square root fit included in figure 7 is very good up to $Re \approx 40$, corresponding to $(Re - Re_c)/Re_c = 1/3$, which is convincing given that we would theoretically expect square-root growth when $(Re - Re_c)/Re_c << 1$. No hysteretic behaviour was observed in either the experimental or numerical results.

E. Characterisation of the instability from simulations

The simulated flow patterns for a wide gap ($g = 5H$) mixing-separating micro-geometry show that a central vortex appears beyond a certain Re_c, and by continuously increasing Re, the vortex divides into two vortices (as shown in figure 6). However, unlike a cross-slot geometry, the transverse velocity component at the central plane of the mixing-separating cell micro-geometry is zero for the entire range of Re tested in the numerical simulations for $g = 5H$. Therefore, to characterise the instability using the simulated data we employ the swirling strength method explained in §III C. This enables us to quantify the strength of the swirling motion as well as identify its position.

Figure 8 shows the variation of the maximum normalised strength of the swirling motion ($\lambda_{ci}H^2/\nu$), on the centre plane $x - y$ ($z = 0$) with Reynolds number. The value of this parameter is zero prior to the formation of the first vortex at $Re_c = 29$, and displays a square root growth near to the instability onset ($30 < Re < 50$) as is expected for a supercritical bifurcation (see inset of figure 8).

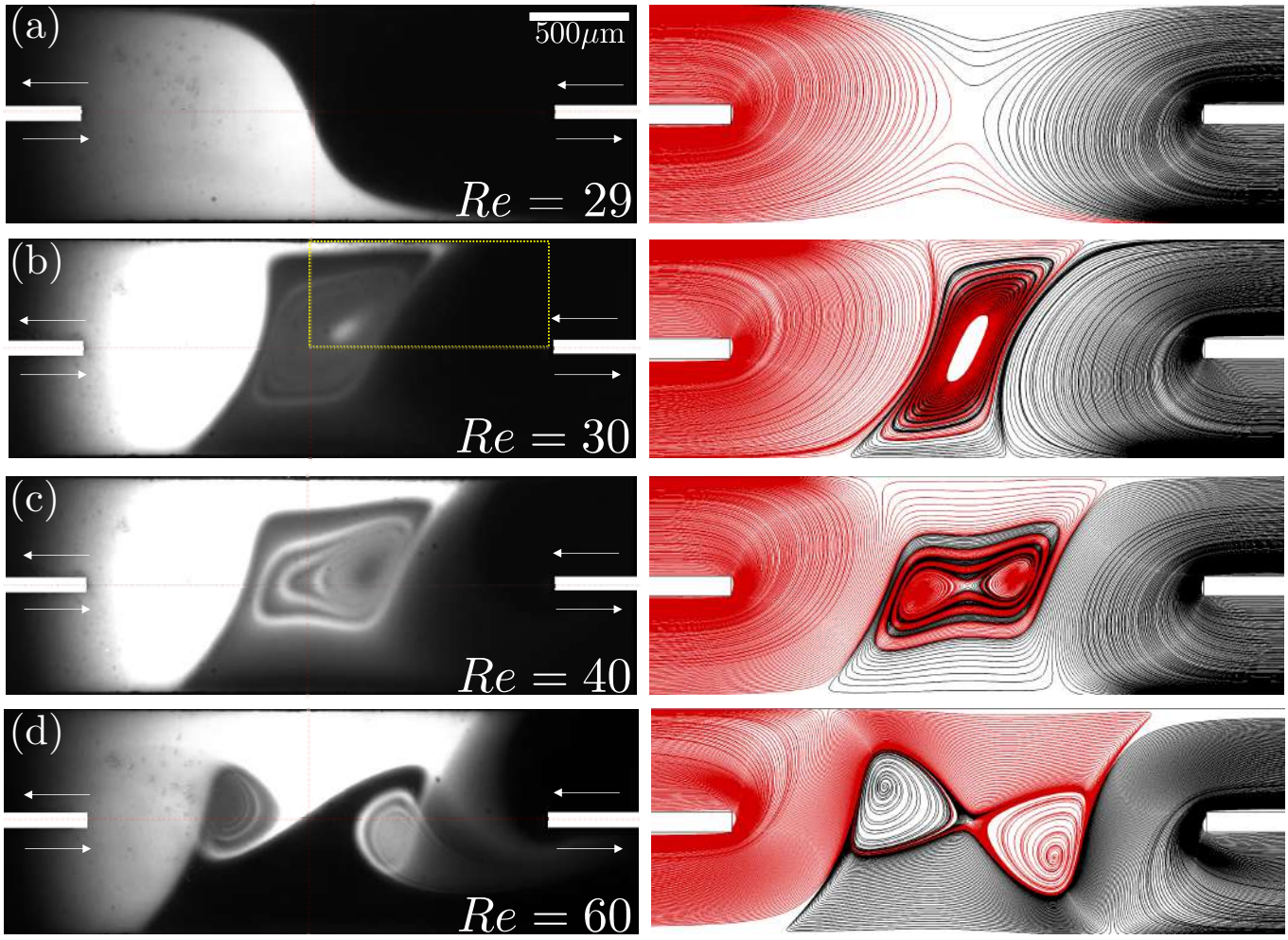

FIG. 6. Experimental flow visualisation (left-hand side) and numerical streamlines (right-hand side) of the flow in the mixing-separating device at different Re. (a) Re=29, before onset of instability; (b) Re=30, single vortex after bifurcation (c) Re=40, two separate co-rotating vortices; (d) Re=60, the distance between the two vortices has increased.

For Reynolds numbers far enough away from onset that the square-root character is not expected ($Re > 50$), the instability parameter continues to grow, but linearly (with a gradient of ≈ 4.6) with Re. This demonstrates that the strength of the vortical motions increases in direct proportion to Re, which is not unexpected as there are no further major changes in flow topology for the range of Re tested ($50 < Re < 185$) using this gap size ($g = 5H$).

The critical Reynolds number found from experiments ($Re_c = 29$) matches the critical Re found from the simulations. In figure 9, the experimental (M) and numerical ($\lambda_{ci,max}H^2/\nu$) results are plotted on the same Re axis. Despite minor differences, and appreciating the fact that the y-axes of the two different bifurcation parameters are necessarily different, the agreement is excellent in terms of the growth of the instability with increasing Re and confirms that the numerical simulations agree with the experimental data. The experimental and numerical data diverge for $Re > 50$ where there is no longer square-root growth of the parameters. This is not surprising as there is no particular reason to expect the strength of the vortex to be intimately linked with the M-parameter beyond the initial growth of the instability and at $Re > 40$ the fluorescence intensity in parts of the region of interest become saturated therefore making any quantitative measure of M somewhat dubious.

In addition to the streamlines shown in figure 6 we can also visualise the flow in the mixing-separating device using our swirling strength bifurcation parameter. Figure 10 depicts the transition from the base flow to the vortical flow regime as the Re changes from 29 to 30. Velocity direction vectors are included in order to show the local direction of the flow and highlight the vortical nature. The colourmap shows the distribution of swirling strength ($\lambda_{ci}H^2/\nu$), which is entirely blank for $Re = 29$ (before the instability) and is seen to clearly highlight the swirling nature of the flow at $Re = 30$ as there is a sudden and dramatic change to the flow topology caused by the onset of the instability.

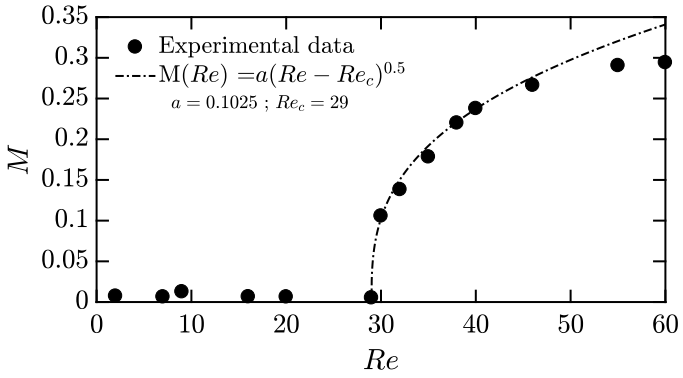

FIG. 7. Characterisation of the instability using the mixing parameter, M, from the experiments, exhibiting the square-root growth expected of a supercritical instability close to onset.

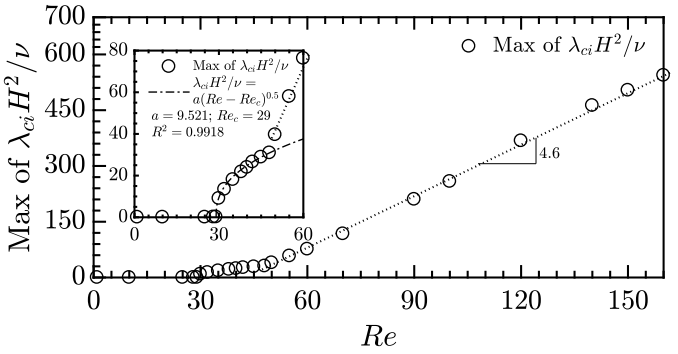

FIG. 8. The variation of the bifurcation parameter used to analyse the numerical data ($\lambda_{ci,max}H^2/\nu$) with Re for $g = 5H$. The critical Reynolds number is 29 and the inset shows a square-root growth near to the instability onset ($30 < Re < 50$). For Re beyond the region of square-root growth, $50 < Re < 185$, the instability parameter grows linearly (with a gradient ≈ 4.6)

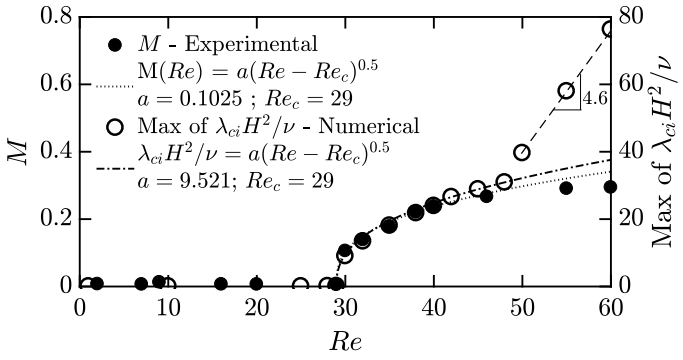

FIG. 9. The variation of the instability growth parameters M (experimental) and $\lambda_{ci,max}H^2/\nu$ (numerical) with Re for $g = 5H$, showing excellent agreement in the region close to onset ($30 < Re < 45$).

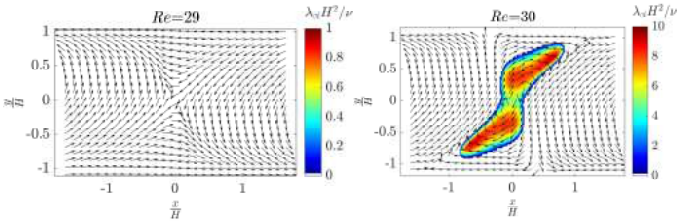

FIG. 10. The change in flow pattern between the base flow (no vortices, $Re = 29$), and the bifurcated flow just after onset (a single large vortex, $Re = 30$) in a mixing separating device with $g = 5H$. The colormap shows the swirling strength ($\lambda_{ci}H^2/\nu$) and the vectors show the direction of the velocity field.

Figure 11 shows how the flow develops beyond Re_c. At $Re = 32$, the single vortex that was present at $Re = 30$ splits into two rotationally-symmetric (through 180°) co-rotating vortices. When near to the onset of the instability, in the region where we still see square-root behaviour ($32 < Re < 50$), these twin vortices change their position as the strength increases with increasing Re. However, in the Re range where the bifurcation parameter shows linear growth $Re > 50$, the vortices do not significantly alter their position, although their shape slightly alters as they get stronger. At $Re = 120$, the vortices appear to merge into a single large vortex, although this does not influence the trend of the strength, which continues to grow linearly with Re.

V. SIMULATIONS INVESTIGATING THE EFFECT OF VARYING THE GAP SIZE (g)

The previous section has demonstrated that the flow in a mixing-separating cell with a wide gap ($g = 5H$) is susceptible to inertial instabilities. The obtained experimental results have served as validation for 3D numerical simulations. In this section we assess the effect of varying the gap size (g) of the mixing-separating device by performing numerical studies using geometries with gaps $g = 2H$, $2.61H$ and $3.86H$ in addition to the previously discussed $g = 5H$. We find that not only is the critical Re of the instability affected by the gap size, but also the nature of the instability and the flow symmetries that are broken.

A. Instability onset for different gap sizes

In section §IV, we showed that the instability in a wide gap ($g = 5H$) mixing-separating microfluidic device is supercritical with $Re_c = 29$. By running identical numerical simulations for different gap sizes we are able to reveal how the Re_c changes as the gap size is decreased. The numerical results, summarised in table III, show that by reducing the gap size the critical Re of the instability that was found to be present in the $g = 5H$ mixing-separating

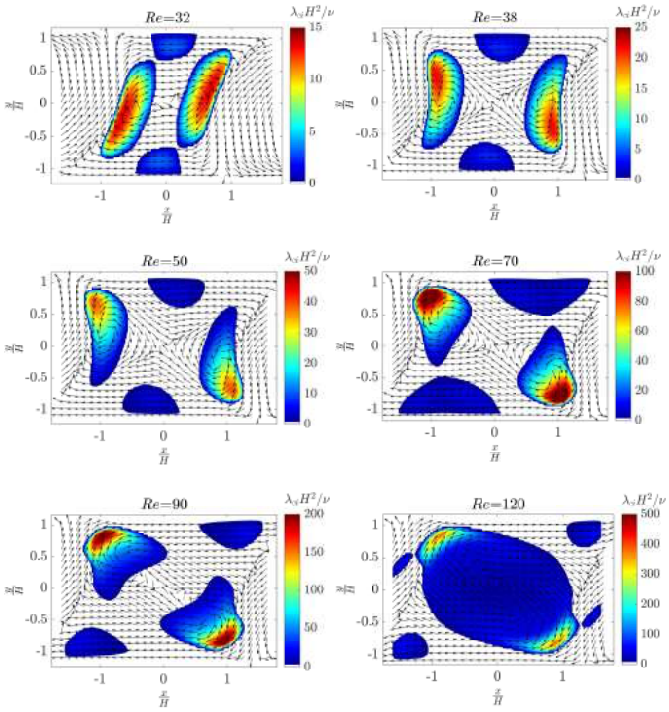

FIG. 11. The evolution of the vortices with Re in a mixing-separating device ($g = 5H$). From $Re = 32$ to $Re = 50$, the cores of the two vortices gradually alter their positions. In the region $50 < Re < 90$, the vortices do not alter their positions significantly. The vortices merge into a single large vortex at $Re = 120$. Rotational symmetry is preserved for all Re. Vectors show the direction of the velocity only.

TABLE III. Critical Reynolds numbers for mixing-separating microfluidic devices with different gap sizes. Two different instabilities (λ_{ci} and w) are possible depending on the gap size. Of the gap sizes tested only $g = 2.61H$ exhibited both types of instability.

g	$2H$	$2.61H$	$3.86H$	$5H$
Re_c (λ_{ci})	–	23	26	29
Re_c (w)	51	84	–	–

device decreases from $Re_c = 29$ at $g = 5H$ to $Re_c = 23$ at $g = 2.61H$. At the smallest gap tested ($g = 2H$) the instability is not present at all. However, at this gap size we observe a different instability at $Re = 51$. This instability is similar to the engulfment instability seen in cross-slot devices[13,14] and T-channels[17–24] in earlier work and the appropriate bifurcation parameter is the maximum transverse velocity (w_{max}/U_b). Of the four gap sizes tested only the $g = 2.61H$ device exhibited both types of instability, with the λ_{ci} instability occurring at a much lower Reynolds number ($Re_c = 23$) than the w instability ($Re_c = 84$).

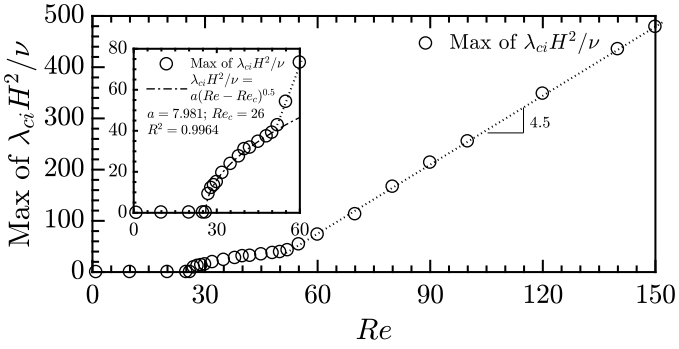

FIG. 12. For a device with a gap size of $3.86H$ the critical Re is 26. Close to the onset, the bifurcation parameter fits a square root function. Similar to a $g = 5H$ gap, when $Re > 50$, the growth of the instability is linear with a gradient ≈ 4.5.

B. Results of simulations with $g = 3.86H$

If the gap size of the mixing-separating device is reduced from $5H$ to $3.86H$, although the critical Re is reduced (from $Re_c = 29$ to $Re_c = 26$), the growth of the instability with Re is very similar as can be seen in figure 12 (when compared to figure 8). The instability is again shown to be supercritical (following a square root near to onset) and away from onset ($Re > 50$) it is linear with a very similar gradient.

Despite the growth of the bifurcation parameter with Re being very similar for $g = 5H$ and $g = 3.86H$ there are some significant differences in the flow fields (compare figure 13 with figures 10 and 11). Below the onset of the instability there is little difference. At $Re = 27$, two vortices appear close to the walls of the mixing-separating cell. This is similar to the $g = 5H$ device at onset, but in the $g = 3.86H$ case the vortices are more distinct from each other. Larger changes ensue as Re is increased. In the $g = 5H$ device there is significant separation of the vortices in the x direction, this is not present in the $g = 3.86H$ device, presumably because of the confinement due to the smaller gap. As such the vortices begin to merge at Re only a little above onset. By $Re = 50$ the vortices have merged into a single large vortex, which then persists largely unchanged at higher Re. (A single large vortex did not appear until $Re = 120$ in the $g = 5H$ device.) It is up until this merging that the bifurcation parameter follows the square-root growth typical of a supercritical instability. After the single large vortex has formed there is linear growth of the strength of the vortex, but no further significant change in the flow topology.

C. Results of simulations with $g = 2.61H$

The device with a gap of $g = 2.61H$ is the only one (of those tested) that exhibits two types of instability. As shown in figure 14, the first instability is the λ_{ci} instability, similar to the $g = 3.86H$ and $g = 5H$ devices,

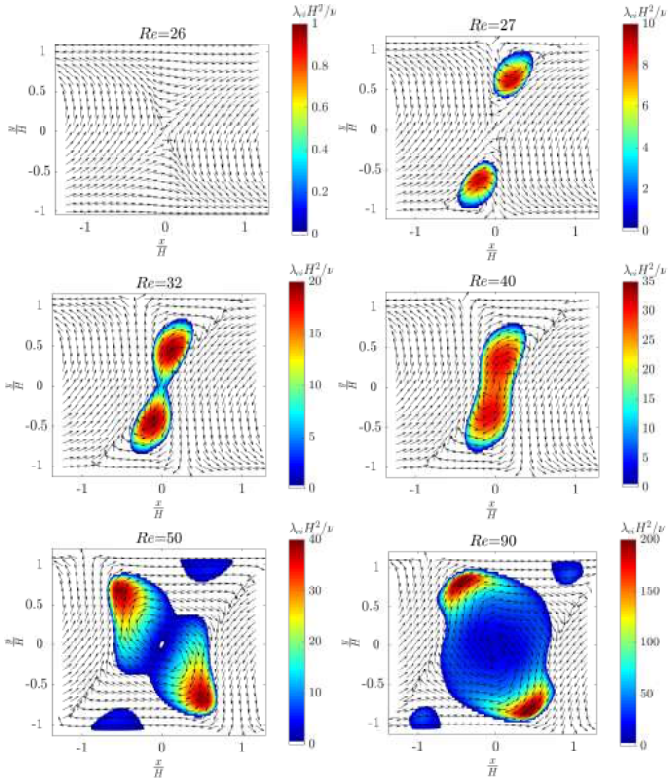

FIG. 13. The evolution of the vortices with Re in a mixing-separating device ($g = 3.86H$). Before the instability there are no vortices ($Re = 26$), at onset two vortices appear ($Re = 27$) and then merge as Re is increased ($27 < Re < 50$). One large vortex, filling most the gap, is formed and persists at higher Re (e.g. $Re = 90$). Rotational symmetry is preserved for all Re. Vectors show the direction of the velocity only.

but occurring slightly earlier at $Re = 23$, and developing with square root growth. This is followed by a linear increase with Re (with a gradient of 4.3), again very similar to the devices with wider gaps. However, at $Re = 84$ this growth stalls and the second instability appears, this time manifested in the transverse velocity component (w), indicating a break of symmetry in the y-z plane. This instability is also supercritical and follows square-root growth until $Re \approx 100$. Beyond this Re the original (λ_{ci}) instability, the strength of which does not grow while the second instability grows, returns to linear growth with the same gradient as it had before the onset of the second instability.

The evolution of the vortices in the y-x plane with Re for the $g = 2.61H$ device (figure 15) is similar to the $g = 3.86H$ device (figure 13). A pair of co-rotating vortices emerge across the gap at onset. These occupy a very similar x location and are separated in the y direction, following the trend previously observed as the gap size is reduced. As Re is further increased the vortices coalesce, after which they broadly remain in a fixed position, their strength increasing. The onset of the second instability (in w_{max}) does not affect the arrangement of the vortices

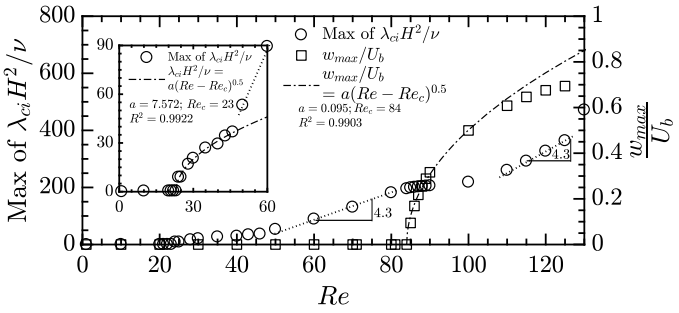

FIG. 14. For a device with a gap size of $2.61H$ the critical Re is 23. Close to the onset, the bifurcation parameter fits a square root function. Similar to the $g = 5H$ and $g = 3.86H$ gaps, when $Re > 50$, the growth of the instability is linear with a gradient ≈ 4.3. At $Re = 84$ the second supercritical instability occurs (seen in the square-root growth of w_{max}/U_b) and interrupts the linear growth of the λ_{ci} parameter until $Re > 100$.

in this plane, although the rate at which their strength increases is slowed whilst the second instability grows.

At $Re > 84$, the bifurcation parameter w_{max}/U_b measured on the $z = 0$ plane being non-zero indicates a breaking of symmetry. This is shown by the streamlines in the $y - z$ plane in figure 16. Prior to this instability the flow (as viewed in this plane) is split into four reflectionally and rotationally symmetric quadrants with no interaction between the streams. The vortices seen at $Re = 84$ in figure 16 are Dean vortices created by the curvature as the stream turns around the corner through the gap. These are not present at very low Re (e.g. $Re = 1$). At the onset of the instability the w-component of velocity on the $z = 0$ plane becomes non-zero and all the reflectional symmetries are broken, although the rotational symmetry (180° about $y = 0$, $z = 0$) is preserved. The instability causes the streams from the two different inlets to interact and by $Re = 90$ fluid from each inlet has entered all four quadrants when it reaches this central plane. Although this instability has been identified using the same bifurcation parameter as is used in the cross-slot device, it is distinctly different from that engulfment instability as it does not result in a single large vortex in the $y - z$ plane. The flow retains the same pattern as shown in figure 16 for $Re = 90$ up to the highest Re that we have tested ($Re = 130$).

D. Results of simulations with $g = 2H$

At the narrowest gap tested ($2H$), the swirling motion at the $x - y$ plane (quantified using $\lambda_{ci}H^2/\nu$), which was observed for all other gap sizes, is completely absent for the entire range of Re tested ($1 < Re < 120$). However, the maximum transverse velocity (w_{max}/U_b) parameter becomes non-zero and fits a square root function near to the critical Reynolds number ($Re_c = 51$). Figure 17 displays both bifurcation parameters, demonstrating that

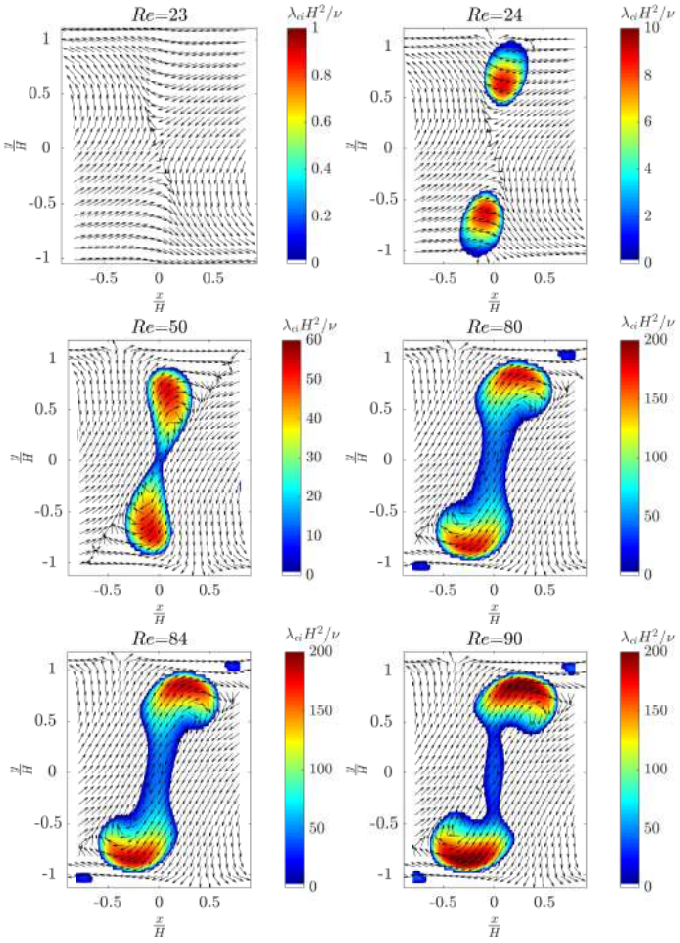

FIG. 15. The evolution of the vortices with Re in a mixing-separating device ($g = 2.61H$). Before the instability there are no vortices ($Re = 23$), at onset two vortices appear ($Re = 24$) and then merge as Re is increased ($Re \approx 50$). One long, slender vortex spanning the channel is formed and persists at higher Re (e.g. $Re > 70$). The onset of the second instability at $Re = 84$ has no significant effect on the vortex in this plane. Rotational symmetry is preserved for all Re. Vectors show the direction of the velocity only.

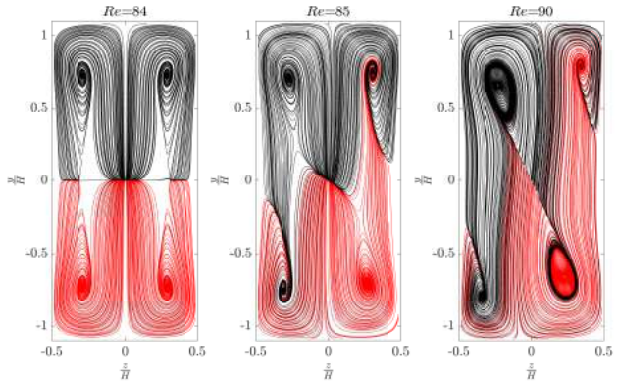

FIG. 16. Streamlines on the $y-z$ plane of the $g = 2.61H$ device before and after onset of the w_{max}/U_b instability. At $Re = 84$ the flow is reflectionally symmetric about $z = 0$ and $y = 0$, at $Re = 85$ the symmetry in both these planes is broken and the w-component of velocity on the $z = 0$ plane is non-zero. The extent of the asymmetry grows as Re is further increased (e.g. see $Re = 90$) although rotational symmetry is preserved throughout. The streamlines are 3D and coloured by the inlet from which they originate, they therefore leave the plane in this 2D plot.

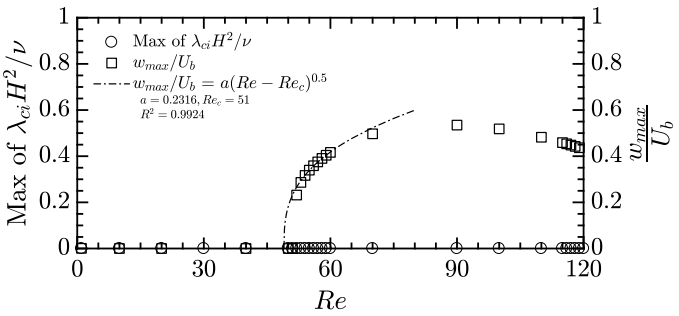

FIG. 17. For the $g = 2H$ geometry there is no instability in λ_{ci}, which is zero for all Re. Instead, the first and only instability is similar to the second instability in the $g = 2.61H$ device, where the w_{max}/U_b parameter highlights a supercritical bifurcation, i.e. it fits a square root function near to onset ($Re_c = 51$) and no hysteresis.

$\lambda_{ci}H^2/\nu$ is always zero and w_{max}/U_b shows supercritical behaviour.

It is worth noting that if two of the arms of a cross-slot device were rotated 90° then it would be a mixing-separating device with $g = \sqrt{2}H$. It is therefore apparent that our mixing-separating device with $g = 2H$ is geometrically closest to the cross-slot device. The only instability that occurs in the mixing-separating device with $g = 2H$ is highly reminiscent of the instability seen in a cross-slot device with aspect ratio of unity. As seen in figure 18, above the onset of the instability a large spiral vortex forms in the y-z plane providing significant mixing of the two fluid streams. This is very similar to the engulfment instability seen in the cross-slot and demonstrates that this instability is not wholly dependent on the specific angle at which the two streams impinge as both 90° (cross-slot) and 180° (mixing-separating) result in a very similar flow (although the instability in the cross-slot is sub-critical for square cross-section channels). In fact, it appears that the size of the gap is a more important parameter (as this instability does not appear at large gap sizes). This presents the question of whether this instability would occur if the flows impinged at other angles between 90° and 180°. It seems logical that it would indeed occur if the gap was small.

Although there is some previous work on the effect of impingement angle[33,34], a full study of devices with a variety of angles and gap sizes is required to answer this question with certainty and to firmly establish how the instability relates to both gap size and impingement angle (which is beyond the scope of this paper). However,

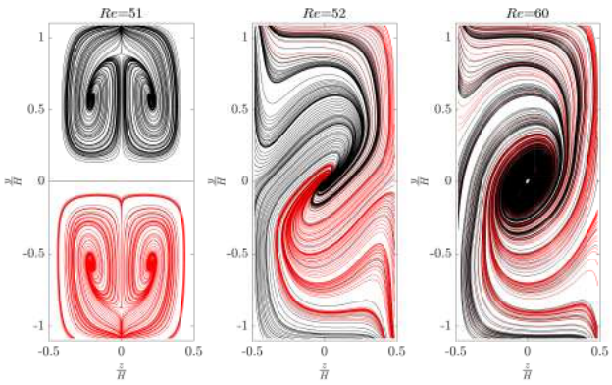

FIG. 18. Streamlines on the $y-z$ plane of the $g = 2H$ device before and after onset of the w_{max}/U_b instability. At $Re = 52$ the reflectional symmetry is broken and the w-component of velocity on the $z = 0$ plane is non-zero. This is an engulfment instability and as Re is further increased (e.g. see $Re = 60$) a large spiral vortex is formed providing significant mixing of the two fluid streams. Rotational symmetry is preserved throughout. The streamlines are 3D and coloured by the inlet from which they originate, they therefore leave the plane in this 2D plot.

the current work indicates that the gap size is of primary importance in determining which instability occurs. As impingement angle and gap size are geometrically dependent upon each other (i.e. if the impingement angle is changed, the gap size is changed as a result of the new angle[33,34]), isolating the effect of the impingement angle and gap size is non-trivial. Therefore our results for the mixing-separating device are useful for reference cases as we can vary the gap size without changing the impingement angle (which is a particular quirk of the *H-geometry*).

VI. SUMMARY AND CONCLUSIONS

A numerical investigation of the flow in mixing-separating (*H-geometry*) microfluidic devices with gap sizes, $g = 2H$, $2.61H$, $3.86H$ and $5H$ has demonstrated that two different inertial instabilities are possible at low Reynolds numbers in the steady flow regime. Which of the two instabilities occurs is primarily dependent on the size of the gap size as well as the Reynolds number (Re). Complementary experiments providing flow visualisations in a mixing-separating device with $g = 5H$ match the results of the numerical simulations very well, providing a validation of the numerical technique, which is applied to additional gap sizes.

The devices with large gaps ($g = 3.86H$ and $g = 5H$) favour the onset of a vortical flow instability in the y-z plane, which we have detected and quantified using swirling strength ($\lambda_{ci}H/\nu$). This instability is seen to be supercritical as its growth follows a square-root close to onset and no hysteresis is apparent. The Re at which the onset first occurs increases as the gap size is increased, but only slightly ($Re = 26$, for $g = 3.86H$ and $Re_c = 29$ for $g = 5H$). This instability also occurs at $g = 2.61H$, but with this gap size a second instability occurs at somewhat higher Re (first instability at $Re = 23$, second at $Re = 84$). The second instability is seen in the transverse velocity component (w_{max}/U_b is used as a bifurcation parameter) and breaks reflectional symmetries similar to a cross-slot device. It too is supercritical as it also follows a square-root close to onset and is not hysteretic. At the smallest gap size tested ($g = 2H$) only the w_{max} instability occurs (at $Re = 51$) and λ_{ci} is zero for all Re tested. This instability is very similar to the cross-slot engulfment instability and a spiral vortex is formed just like in the cross-slot flow.

The work provides a greater understanding of the instabilities in these mixing-separating microfluidic devices through the characterisation of the flow over a range of Re for several gap sizes. In particular the strong dependence of the instability on gap size is revealed. The similarity of the instability in the small gap-size *H-geometry* to the more extensively studied cross-slot brings into question the importance of the geometrical arrangement in these devices as a very similar flow can be achieved with the inlet arms parallel or perpendicular to the outlet arms. This perhaps reveals a route to designing more compact devices and is an indication that gap size is a more important design parameter than impingement angle. In any case, we provide a database that highlights the importance of gap size in the design of such devices and provides information regarding the onset Re of two types of inertial instabilities over a range of gap sizes which are viable choices for microfluidic applications.

ACKNOWLEDGMENTS

AFD would like to thank the financial support from the National Council of Scientific and Technologic Development in Brazil (CNPq) and the Brazilian Ministry of Education for his PhD research grant (under number 203195/2014-0). He also would like to thank Dr Waleed M. Abed and Mahdi Davoodi for helpful discussions. RJP acknowledges EPSRC for the award of a fellowship under grant number EP/M025187/1.

[1] C.-Y. Lee, C.-L. Chang, Y.-N. Wang, and L.-M. Fu, "Microfluidic mixing: a review," Int. J. Mol. Sci. **12**, 3263–3287 (2011).
[2] D. D. Carlo, "Inertial microfluidics," Lab. Chip **9**, 3038–3046 (2009).
[3] B. Ivorra, J. López Redondo, A. M. Ramos, and J. G. Santiago, "Design sensitivity and mixing uniformity of a micro-fluidic mixer," Phys. Fluids **28**, 012005 (2016).
[4] E. Kaliviotis, J. M. Sherwood, and S. Balabani, "Local viscosity distribution in bifurcating microfluidic blood flows," Phys. Fluids **30**, 030706 (2018).
[5] A. D. Stroock, S. K. Dertinger, A. Ajdari, I. Mezic, H. A. Stone, and G. M. Whitesides, "Chaotic mixer for microchannels," Science (New York, N.Y.) **295**, 647–651 (2002).
[6] H. Haddadi and D. D. Carlo, "Inertial flow of a dilute suspension

over cavities in a microchannel," J. Fluid Mech. **811**, 436–467 (2017).
[7]D. Bothe, C. Stemich, and H.-J. Warnecke, "Fluid mixing in a T-shaped micro-mixer," Chem. Eng. Sci. **61**, 2950–2958 (2006).
[8]J. Eustice, "Experiments on stream-line motion in curved pipes," Proceedings of the Royal Society of London - A **85**, 119–131 (1911).
[9]V. N. Kalashnikov and M. Tsiklauri, "Ordered three-dimensional structures resulting from instability of two-dimensional flow in crossed channels," Fluid Dyn. **26**, 161–165 (1991).
[10]V. N. Kalashnikov and M. Tsiklauri, "Effect of polymer additives on ordered three-dimensional structures arising in cross-slot flow," J. Non-Newtonian Fluid Mech. **48**, 215–223 (1993).
[11]K.-W. Hsiao, J. Dinic, Y. Ren, V. Sharma, and C. M. Schroeder, "Passive non-linear microrheology for determining extensional viscosity," Phys. Fluids **29**, 121603 (2017).
[12]G. Dockx, T. Verwijlen, W. Sempels, M. Nagel, P. Moldenaers, J. Hofkens, and J. Vermant, "Simple microfluidic stagnation point flow geometries," Biomicrofluidics **10**, 043506 (2016).
[13]S. J. Haward, R. J. Poole, M. A. Alves, P. J. Oliveira, N. Goldenfeld, and A. Q. Shen, "Tricritical spiral vortex instability in cross-slot flow," Physical Review E **93**, 031101 (2016).
[14]W. M. Abed, A. F. Domingues, R. J. Poole, and D. J. C. Dennis, "Heat transfer enhancement in a cross-slot micro-geometry," Int. J. Therm. Sci. **121**, 249–265 (2017).
[15]K. Malecha, L. J. Golonka, J. Baldyga, M. Jasinska, and P. Sobieszuk, "Serpentine microfluidic mixer made in LTCC," Sens. Actuators, B **143**, 400–413 (2009).
[16]H. Haddadi, H. Naghsh-Nilchi, and D. D. Carlo, "Separation of cancer cells using vortical microfluidic flows," Biomicrofluidics **12**, 014112 (2018).
[17]M. Engler, N. Kockmann, T. Kiefer, and P. Woias, "Numerical and experimental investigations on liquid mixing in static micromixers," Chemical Engineering Journal **101**, 315–322 (2004).
[18]S. H. Wong, M. C. Ward, and C. W. Wharton, "Micro T-mixer as a rapid mixing micromixer," Sens. Actuators, B **100**, 359–379 (2004).
[19]N. Kockmann, T. Kiefer, M. Engler, and P. Woias, "Convective mixing and chemical reactions in microchannels with high flow rates," Sens. Actuators, B **117**, 495–508 (2006).
[20]A. Soleymani, E. Kolehmainen, and I. Turunen, "Numerical and experimental investigations of liquid mixing in T-type micromixers," Chemical Engineering Journal **135**, S219–S228 (2008).
[21]S. Dreher, N. Kockmann, and P. Woias, "Characterization of laminar transient flow regimes and mixing in T-shaped micromixers," Heat Transfer Eng. **30**, 91–100 (2009).
[22]S. Thomas and T. A. Ameel, "An experimental investigation of moderate reynolds number flow in a T-channel," Exp. Fluids **49**, 1231–1245 (2010).
[23]M. Hoffmann, M. Schluter, and N. Rabiger, "Micro and macro mixing: Analysis, simulation and numerical calculation," (Springer-Verlag Berlin Heidelberg, Heat and Mass Transfer, 2010) pp. 287–303.
[24]R. J. Poole, M. Alfateh, and A. Gauntlett, "Bifurcation in a T-channel junction: Effects of aspect ratio and shear-thinning," Chem. Eng. Sci. **104**, 839–848 (2013).
[25]J. Soulages, M. S. N. Oliveira, P. C. Sousa, M. A. Alves, and G. H. McKinley, "Investigating the stability of viscoelastic stagnation flows in T-shaped microchannels," J. Non-Newtonian Fluid Mech. **163**, 9–24 (2009).
[26]R. J. Poole, G. N. Rocha, and P. J. Oliveira, "A symmetry-breaking inertial bifurcation in a cross-slot flow," Computers and Fluids **93**, 91–99 (2014).
[27]S. Sarkar, K. Singh, V. Shankar, and K. Shenoy, "Numerical simulation of mixing at 1-1 and 1-2 microfluidic junctions," Chem. Eng. Process. Process Intensif. **85**, 227–240 (2014).
[28]S. J. Haward, M. S. N. Oliveira, M. A. Alves, and G. H. McKinley, "Optimized cross-slot flow geometry for microfluidic extensional rheometry," Phys. Rev. Lett. **109** (2012).
[29]T. M. Squires and S. R. Quake, "Microfluidics: Fluid physics at the nanoliter scale," Rev. Mod. Phys. **77**, 977 (2005).
[30]F. J. Galindo-Rosales, M. A. Alves, and M. S. Oliveira, "Microdevices for extensional rheometry of low viscosity elastic liquids: a review," Microfluid. Nanofluid. **14**, 1–19 (2013).
[31]K. Zografos, N. Burshtein, A. Q. Shen, S. J. Haward, and R. J. Poole, "Elastic modifications of an inertial instability in a 3D cross-slot," J. Non-Newtonian Fluid Mech. (2018).
[32]N. Burshtein, K. Zografos, A. Q. Shen, R. J. Poole, and S. J. Haward, "Inertioelastic flow instability at a stagnation point," Phys. Rev. X **7**, 041039 (2017).
[33]M. Cachile, L. Talon, J. M. Gomba, J. P. Hulin, and H. Auradou, "Stokes flow paths separation and recirculation cells in X-junctions of varying angle," Phys. Fluids **24**, 021704 (2012).
[34]P. Correa, J. MacIntyre, J. Gomba, M. Cachile, J. Hulin, and H. Auradou, "Three-dimensional flow structures in X-shaped junctions: Effect of the Reynolds number and crossing angle," Physics of Fluids **31**, 043606 (2019).
[35]T. Cochrane, K. Walters, and M. F. Webster, "On Newtonian and non-Newtonian flow in complex geometries," Philosophical Transactions of the Royal Society of London A: Mathematical, Physical and Engineering Sciences **301**, 163–181 (1981).
[36]K. Walters and M. F. Webster, "On dominating elastico-viscous response in some complex flows," Philosophical Transactions of the Royal Society of London A: Mathematical, Physical and Engineering Sciences **308**, 199–218 (1982).
[37]J. A. C. Humphrey and S. Li, "Tilting, stretching, pairing and collapse of vortex structures in confined counter-current flow," Journal of Fluids Engineering, ASME **103**, 466–470 (1981).
[38]J. A. C. Humphrey, J. L. Rosales, L. A. Legendre, J. P. LeDuc, and J. P. Landers, "Vortex dynamics in confined counter-current shearing flows with applications to mixing," Int. J. Heat Fluid Flow **29**, 1089–1102 (2008).
[39]F. Durst, S. Ray, B. Unsal, and O. A. Bayoumi, "The development lengths of laminar pipe and channel flows," Journal of Fluids Engineering, Transactions of the ASME , 1154–1160.
[40]J. Judy, D. Maynes, and B. Webb, "Characterization of frictional pressure drop for liquid flows through microchannels," Int. J. Heat Mass Transfer **45**, 3477–3489 (2002).
[41]M. E. Steinke and S. G. Kandlikar, "Single-phase liquid friction factors in microchannels," Int. J. Therm. Sci. **45**, 1073–1083 (2006).
[42]D. Ross, M. Gaitan, and L. E. Locascio, "Temperature measurement in microfluidic systems using a temperature-dependent fluorescent dye," Anal. Chem. **73**, 4117–4123 (2001).
[43]C.-Y. Huang, C.-A. Li, H.-Y. Wang, and T.-M. Liou, "The application of temperature-sensitive paints for surface and fluid temperature measurements in both thermal developing and fully developed regions of a microchannel," J. Micromech. Microeng. **23**, 037001 (2013).
[44]C.-Y. Huang, C.-A. Li, B.-H. Huang, and T.-M. Liou, "The study of temperature rise in a 90-degree sharp bend microchannel flow under constant wall temperature condition," Journal of Mechanics **30**, 661–666 (2014).
[45]ANSYS, ANSYS Fluent User's Guide (2011).
[46]S. V. Patankar and D. B. Spalding, "A calculation procedure for heat, mass and momentum transfer in three-dimensional parabolic flows," Int. J. Heat Mass Transfer **15**, 1787–1806 (1972).
[47]J. Zhou, R. J. Adrian, S. Balachandar, and T. M. Kendall, "Mechanisms for generating coherent packets of hairpin vortices in channel flow," J. Fluid Mech. **387**, 353–396 (1999).
[48]W. M. Abed, R. D. Whalley, D. J. C. Dennis, and R. J. Poole, "Numerical and experimental investigation of heat transfer and fluid flow characteristics in a micro-scale serpentine channel," Int. J. Heat Mass Transfer **88**, 790–802 (2015).
[49]R. K. Shah and A. L. London, Laminar flow forced convection in ducts (Academic press, 2014).